

ANALYSIS OF THE RADIOMETRIC RESPONSE OF ORANGE TREE CROWN IN HYPERSPECTRAL UAV IMAGES

N. N. Imai^{1,2,*}, E. A. S. Moriya¹, E. Honkavaara³, G. T. Miyoshi², M. V. A. de Moraes¹, A. M. G. Tommaselli^{1,2}, R. Näsi³

¹Dept. of Cartography, São Paulo State University (UNESP), Presidente Prudente-SP, Brazil - (nimai, tomaseli)@fct.unesp.br, (erikaasaito, antunesdemoraes)@gmail.com

²Post Graduate Program in Cartographic Science, São Paulo State University (UNESP), Presidente Prudente-SP, Brazil - takahashi.gabi@gmail.com

³Finnish Geospatial Research Institute FGI, Geodeetinrinne 2, P.O. Box 15, FI-02431 Masala, Finland - (eija.honkavaara, roope.nasi)@nls.fi

KEY WORDS: radiometric calibration; hyperspectral image; bidirectional reflectance distribution function (BRDF); trend analysis, UAV, high spectral and spatial resolution remote sensing.

Commission III, WG III/4

ABSTRACT:

High spatial resolution remote sensing images acquired by drones are highly relevant data source in many applications. However, strong variations of radiometric values are difficult to correct in hyperspectral images. Honkavaara et al. (2013) presented a radiometric block adjustment method in which hyperspectral images taken from remotely piloted aerial systems – RPAS were processed both geometrically and radiometrically to produce a georeferenced mosaic in which the standard Reflectance Factor for the nadir is represented. The plants crowns in permanent cultivation show complex variations since the density of shadows and the irradiance of the surface vary due to the geometry of illumination and the geometry of the arrangement of branches and leaves. An evaluation of the radiometric quality of the mosaic of an orange plantation produced using images captured by a hyperspectral imager based on a tunable Fabry-Pérot interferometer and applying the radiometric block adjustment method, was performed. A high-resolution UAV based hyperspectral survey was carried out in an orange-producing farm located in Santa Cruz do Rio Pardo, state of São Paulo, Brazil. A set of 25 narrow spectral bands with 2.5 cm of GSD images were acquired. Trend analysis was applied to the values of a sample of transects extracted from plants appearing in the mosaic. The results of these trend analysis on the pixels distributed along transects on orange tree crown showed the reflectance factor presented a slightly trend, but the coefficients of the polynomials are very small, so the quality of mosaic is good enough for many applications.

1. INTRODUCTION

Spatial and spectral high resolution remote sensing images acquired from drones are a source of information of high degree of relevance, but the variations of Digital Number - DN introduced in these kind of images make their correction very difficult.

Variations of radiometric measurements in remote sensing images are caused by several factors related to the physical environment. The anisotropy of the spectral response of targets is a result of its Bidirectional Reflectance Distribution Function - BRDF. The BRDF effects introduce variations in radiance measured in different acquisition and lighting geometries (Peltoniemi et al. 2007, Markelin et al. 2008, Honkavaara et al. 2012). This anisotropy combined with the variation of the irradiance of these targets produces variations in the radiometric values, which are undesirable for many applications. This type of problem has been addressed by several researchers, which are interested in the plant cover information (Li and Strahler 1986, Vermote et al. 2009, Bréon and Vermote 2012). Alternatives to perform radiometric correction of aerial images taken from piloted and remotely piloted aerial systems (RPAS) have been more recently developed (Pros et al. 2013).

Radiometric correction approaches of multispectral and hyperspectral images taken from RPAS have been developed mainly for applications in agriculture where the canopies are frequently almost flat. In Brazil, mechanized annual crops surfaces, as well as sugarcane cultivation have this kind of geometry. However, some permanent crops, such as those for the production of orange, lemon, mango, coffee, among others, have a canopy in which the tops of the plants and the lines between them form a mosaic that creates a 3D texture.

There is a great interest in the development of imaging systems to monitor these crops, as this kind of system can produce images which have great potential for detecting diseases as well as nutritional plants deficiency. However, the radiometric and geometric correction of images acquired at low altitude with RPAS of this type of target remains a complex task, mainly due to the effects of the micro relief generated by the trees canopies. Images taken at low altitude, with ground sample distance (GSD) around 10 cm or smaller have high frequency variations both in geometry and radiometry.

Jakob et al. (2017) presented a solution for the geometric and radiometric calibration of high spatial resolution images with a GSD of 3.25 cm in rugged regions with low density of vegetation cover, since mineral prospecting was the subject of interest in this job. The main problem faced in that work was the high variation of the micro-relief. Honkavaara et al. (2013) presented

a solution in which hyperspectral images taken from RPAS were processed both geometrically and radiometrically to produce a georeferenced mosaic in which the standard Reflectance Factor for the nadir is represented. A bundle block adjustment was used to estimate orientation parameters followed by digital surface model generation, which were the start point of the proposed algorithm. Following, illumination correction and a BRDF correction based on the model developed by Walthall et al. (1985) were applied to correct the anisotropy effects. Variations of the solar illumination and other disturbances can be corrected by different approaches, including measures of irradiance in a sensor placed over the RPAS, or by a cosine sensor in the terrain. It is also feasible to model factors causing radiometric differences between overlapping images (illumination variations, BRDF, and other effects) and to use a radiometric block adjustment to calculate model parameters that minimize radiometric differences between images.

The plant crowns in permanent cultivation show complex variations since the density of shadows and the irradiance of the surface vary due to the geometry of illumination and the geometry of the arrangement of branches and leaves. The shape of the plant crowns can be roughly modelled by a digital surface model (DSM). The spectral reflectance factor can be estimated for the nadir position based on this DSM and the illumination geometry. In this sense, despite the solution proposed by Honkavaara et al. (2013) had been optimized for nearly flat canopy crop field, it can also be used for orange production fields.

In this work, an evaluation of the radiometric quality of the mosaic of an orange plantation produced using images captured by a hyperspectral imager based on a tunable Fabry-Pérot interferometer (FPI) and applying the method by Honkavaara et al. (2013), is presented. Considering that a healthy plant should present only random variations around its average reflectance factor over its crown, a trend analysis was performed based on observations extracted from a sample of transects to check the hypothesis that the spatial distribution of the values may show spatial tendency.

1.1 Study area

The study area is an orange production farm which belongs to the AGROTENAS which is a partner company in the development of this work. It is located in Guacho farm, city of Santa Cruz do Rio Pardo in the Sao Paulo State, Brazil. Figure 1 shows the location of this area. The coordinates of the study area in the WGS84 system are 22°47'42.14"S and 49°23'46.28"W. The aerial and field surveys were carried out on March 22, 2017.

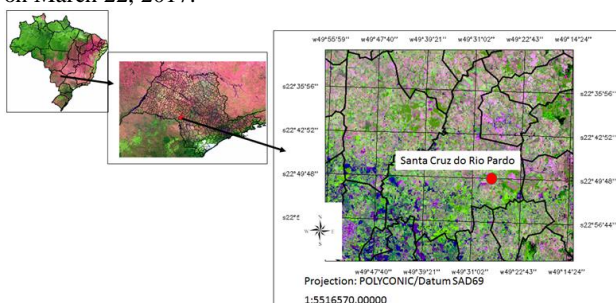


Figure 1. Guacho farm in the city of Santa Cruz do Rio Pardo. City of Santa Cruz do Rio Pardo in Sao Paulo State and in Brazil.

The area which was imaged is shown in Figure 2.

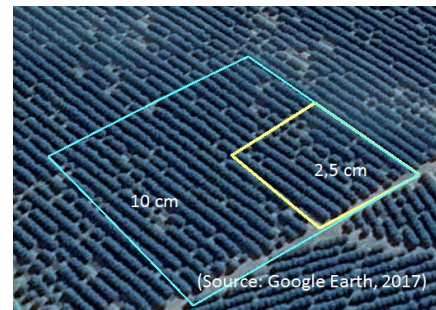


Figure 2. Aerial surveyed area is the yellow polygon region.

2. METHODOLOGY

The analysis of the radiometric quality of an orange production plantation, more specifically the radiometric quality on the top of the plant was developed according to the following steps: i) Image acquisition; ii) Dark current correction and radiometric calibration; iii) Geometric processing with bundle block adjustment; iv) Radiometric block adjustment; v) Tree delimitation; vi) transect design on the top of sample plants; vii) Analysis of variance applied on the squared residuals of polynomial regression and the average calculated from each transects pixels.

2.1 Image acquisition

The Rikola Hyperspectral Camera, Figure 3a, a hyperspectral imagery sensor developed by Senop Ltd. (<http://senop.fi/>) was used for image acquisition. This camera has two complementary metal oxide semiconductor (CMOS) frame sensors based on the FPI (Oliveira et al., 2016). It is able to acquire images from the visible to the near-infrared (VIS-NIR) and one or two spectral bands simultaneously. In addition, the camera can be connected to a global positioning system (GPS).

A quadcopter RPAS was equipped with this FPI spectral camera, Figure 3b, which was configured to acquire 25 narrow spectral bands with 2.5 cm GSD with flight height of 36 m.

The Rikola Camera was configured to take images in the spectral bands centred on the following wavelengths, with Full Width Half Maximum (FWHM) showed in parenthesis, both in nm: 505.37 (9.51); 519.69 (23.78); 550.34 (23.36); 559.53 (20.69); 584.59 (21.74); 594.61 (21.94); 614.78 (20.61); 630.29 (19.6); 650.09 (19.39); 659.72 (16.83); 669.75 (19.8); 679.84 (20.45); 690.28 (18.87); 700.28 (18.94); 710.06 (19.7); 720.17 (19.31); 729.57 (19.01); 740.42 (17.98); 750.16 (17.97); 759.62 (18.86); 769.89 (18.72); 779.68; (17.51); 800.43 (17.75); 819.66 (17.84).

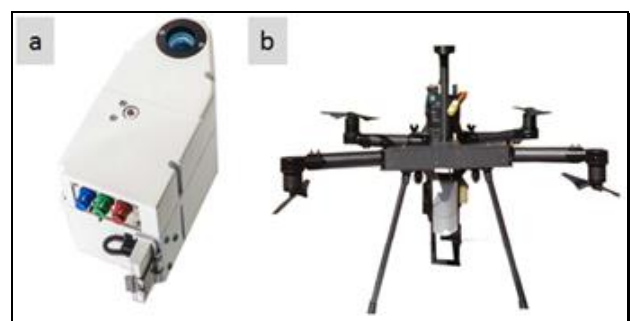


Figure 3. a) Rikola Hyperspectral Camera; b) quadcopter RPAS equipped with the Rikola Hyperspectral camera

2.2 Image processing

Dark current correction was performed using a dark image acquired before the flight, and the radiometric calibration using a calibration file provided by the manufacturer both on the images acquired. The Hyperspectral Imager software provided by Senop Ltd was used for both procedures.

The Interior Orientation Parameters (IOP) were estimated using the on-job calibration, performed with AgiSoft PhotoScan in order to reconstruct the camera geometry. This AgiSoft PhotoScan was used to refine the Exterior Orientation Parameters (EOP) of three reference bands, for image orientation. The reference bands were centred in 559.53 nm, 679.84 nm and 769.89 nm. The GNSS GPS sensor from the camera was used to estimate the initial images position.

Then, a DSM of the area with 2.5 cm of GSD was produced by dense matching method with AgiSoft PhotoScan as well. The BRDF and illumination variation caused by differences in the geometry of illumination and viewing during the imaging acquisition were corrected by applying the method proposed and presented by Honkavaara et al. (2013), Hakala et al. (2013) and Näsi et al. (2016).

As the last step in the mosaic production process it is necessary to transform DN to physical values in the images. In this sense, the empirical line method (Smith and Milton, 1999) was applied. Black, grey and white targets were placed in the study area to be used as radiometric reference. Figure 4 shows targets used in the hyperspectral image mosaic production: (A) Targets for geometric correction, (b) Targets for radiometric correction.

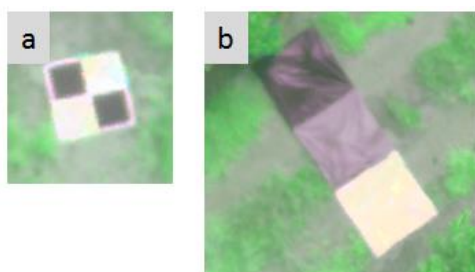


Figure 4. a) Targets for geometric correction, b) Targets for radiometric correction.

2.3 Trend analysis

It was drawn lines at the top of the orange plant samples to choose samples of pixels to be evaluated. These samples of pixels were used to evaluate the radiometric variation of the mosaic spectral reflectance of the pixels along these trajectories. Therefore, it was drawn four directions on each crown of orange plant in order to check the spectral reflectance factor variation along all of these geometries. Figure 5 shows all lines which were adopted to choose the pixels of the sample transect. The wavelengths sampled were two in the visible and two in the near-infrared since that each pair of bands are acquired by different sensor in the camera. The bands centres adopted to develop the analysis were: 550 nm and 660 nm in the visible spectral region and 720 nm, 800 nm in the near-infrared. Thus, images acquired by each sensor were evaluated.

Trend analysis was applied to the values of a sample of transects extracted from plants appearing in the mosaic. It is not expected that there is a trend in the energy values reflected at any wavelength of a healthy plant crown transect, but only random variations around the mean. Considering the flat hemisphere shape of the crown of an orange tree, it was decided to limit the evaluations for linear and quadratic (parabolic) spatial trends. This trend analysis is based on parameters presented in Table 1.

Source of variation	Squared sum	D.F.	Squared mean	Fc
Polynomial regression	SQP	m	$SQP/m = MQP$	
Residuals	SQR	n-m-1	$SQR/(n-m-1) = MQR$	
Total	SQT	n-1	$SQT/(n-1) = MQT$	

Where: DF = Degrees of freedom, m = polynomial regression freedom degree, n = sample number, H0 = spatial trend is accepted, H1 = trend is not accepted. Residuals are independent among them, then: $SQP = SQT - SQR$.

Table 1. Variance analysis table (ANOVA - Analysis Of Variance).

3. RESULTS AND ANALYSIS

Figure 5 shows the transects on the crown of orange plants and where are the pixels of the sample to be analysed.

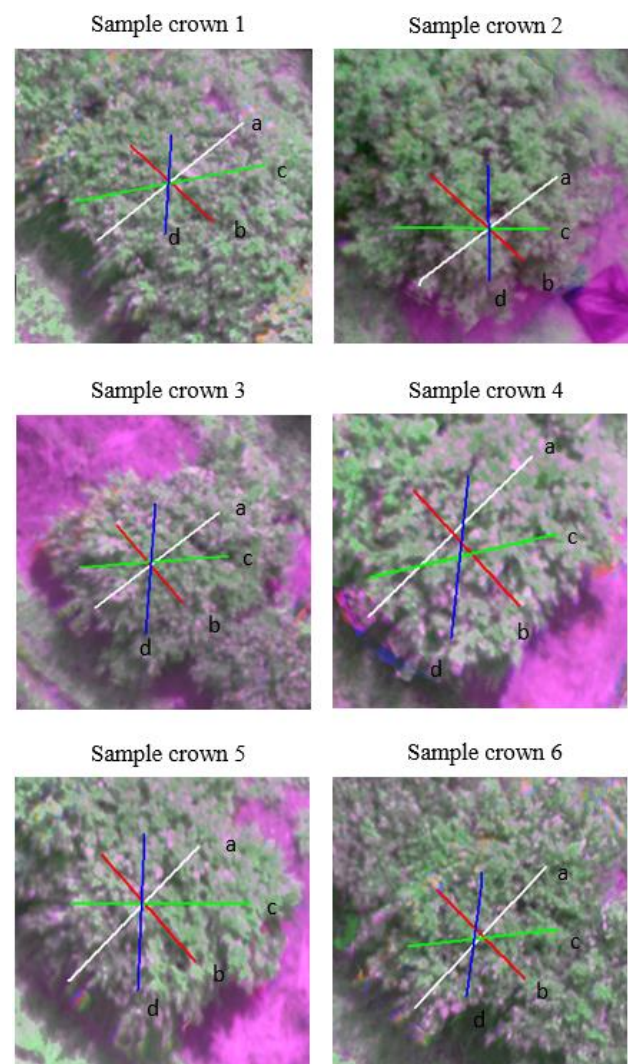


Figure 5. Transects where pixel values were extracted.

Figure 5 shows four transects along each of the 6 crowns sampled. The average was calculated for the pixels of each one with the values of spectral reflectance factor in each of the four wavelengths analysed and the residuals as well. A linear and a quadratic polynomial equation were adjusted based on minimum of the square error.

The parameters: mean, standard deviation and sum of square are presented in the table 2.

sample	Transect	λ (nm)	mean	stdev	Sum of square
1	a	550	0.0910	0.0521	1.5260
1	a	660	0.5342	0.1182	41.5963
1	a	720	0.4425	0.1054	28.7468
1	a	800	0.5957	0.1119	51.0538
1	b	550	0.0415	0.0522	0.3524
1	b	660	0.4061	0.2034	16.4653
1	b	720	0.3344	0.1637	11.0648
1	b	800	0.4948	0.1587	21.5797
1	c	550	0.0716	0.0440	1.2697
1	c	660	0.5182	0.1323	51.4670
1	c	720	0.4337	0.1226	36.5524
1	c	800	0.5769	0.1201	62.4819
1	d	550	0.0658	0.0321	0.5185
1	d	660	0.5193	0.1113	27.3481
1	d	720	0.4324	0.0970	19.0341
1	d	800	0.5942	0.1003	35.2095
2	a	550	0.0119	0.0256	0.0929
2	a	660	0.1345	0.1257	3.9486
2	a	720	0.1852	0.1303	5.9847
2	a	800	0.2460	0.1071	8.4113
2	b	550	0.0110	0.0246	0.0554
2	b	660	0.1547	0.1350	3.2282
2	b	720	0.2101	0.1375	4.8364
2	b	800	0.2588	0.1117	6.1059
2	c	550	0.0006	0.0219	0.0603
2	c	660	0.0878	0.1193	2.7741
2	c	720	0.1385	0.1016	4.2339
2	c	800	0.2069	0.1010	6.7211
2	d	550	0.0128	0.0241	0.0755
2	d	660	0.1342	0.1164	3.2055
2	d	720	0.1812	0.1211	4.8294
2	d	800	0.2393	0.1025	6.9023
3	a	550	0.0617	0.0494	0.7217
3	a	660	0.4630	0.1956	29.2701
3	a	720	0.3329	0.1533	15.5564
3	a	800	0.5154	0.1602	33.7626
3	b	550	0.0443	0.0344	0.2345
3	b	660	0.4401	0.1705	16.6753
3	b	720	0.3217	0.1233	8.8845
3	b	800	0.5065	0.1234	20.3632
3	c	550	0.0559	0.0426	0.6792
3	c	660	0.4403	0.1721	30.8097
3	c	720	0.3102	0.0122	16.0990
3	c	800	0.4901	0.1512	36.2822
3	d	550	0.0532	0.0425	0.5687
3	d	660	0.4499	0.1907	29.3318
3	d	720	0.3257	0.1425	15.5221
3	d	800	0.5076	0.1333	33.8617
4	a	550	0.0762	0.0566	1.3032
4	a	660	0.4894	0.1876	39.7929
4	a	720	0.2743	0.1295	13.3254
4	a	800	0.5637	0.1628	49.8840
4	b	550	0.0829	0.0375	0.7773
4	b	660	0.5077	0.1420	26.1087
4	b	720	0.2725	0.1010	7.9293
4	b	800	0.5661	0.1253	31.5800
4	c	550	0.0715	0.0465	1.1972
4	c	660	0.5591	0.1724	56.4419
4	c	720	0.3138	0.1178	18.5223

4	c	800	0.6060	0.1532	64.4404
4	d	550	0.0722	0.0512	0.9693
4	d	660	0.4898	0.1442	32.3087
4	d	720	0.2663	0.1025	10.0891
4	d	800	0.5496	0.1220	39.2812
5	a	550	0.0558	0.0471	0.6216
5	a	660	0.3824	0.1841	21.0425
5	a	720	0.3000	0.1660	13.7257
5	a	800	0.4853	0.1758	31.1351
5	b	550	0.0721	0.0505	0.6480
5	b	660	0.4756	0.1550	20.9945
5	b	720	0.3668	0.1257	12.6152
5	b	800	0.5495	0.1434	27.0718
5	c	550	0.0841	0.0497	1.5054
5	c	660	0.5407	0.1431	49.4094
5	c	720	0.4301	0.1245	31.6680
5	c	800	0.6172	0.1248	62.6377
5	d	550	0.0914	0.0617	1.4179
5	d	660	0.4756	0.1781	30.1457
5	d	720	0.3635	0.1448	17.8881
5	d	800	0.5559	0.1513	38.8084
6	a	550	0.0391	0.0427	0.3998
6	a	660	0.3874	0.1851	22.0897
6	a	720	0.3213	0.1680	15.7471
6	a	800	0.4787	0.1598	30.5406
6	b	550	0.0529	0.0260	0.2806
6	b	660	0.5190	0.1183	22.9403
6	b	720	0.4378	0.1088	16.4697
6	b	800	0.5814	0.1162	28.4580
6	c	550	0.0377	0.0368	0.3784
6	c	660	0.4361	0.1773	30.3235
6	c	720	0.3778	0.1694	23.4567
6	c	800	0.5289	0.1580	41.7135
6	d	550	0.0469	0.0450	0.4371
6	d	660	0.4594	0.1692	24.9003
6	d	720	0.3803	0.1575	17.5978
6	d	800	0.5231	0.1522	30.8399

Table 2. Mean, Standard deviation and Sum of square errors of the samples crowns spectral reflectance factor of the pixels along transects.

Polynomial adjustment results are presented in Table 3.

λ (nm)/ Sample	Linear polynomial			Quadratic polynomial			
	a0	a1	Res.	a0	a1	a2	Res.
1a	0.076	2.2E-04	0.364	0.078	1.4E-04	1.0E-06	0.363
	0.103	-1.5E-03	0.116	0.103	-1.5E-03	0.0E+00	0.116
	0.030	4.6E-04	0.243	0.052	-2.7E-04	4.0E-06	0.226
	0.075	-1.9E-04	0.096	0.082	-6.1E-04	4.0E-06	0.095
1b	0.567	4.6E-04	1.879	0.506	2.1E-03	-1.9E-05	1.780
	0.671	-6.5E-03	1.443	0.587	-4.1E-04	-7.6E-05	1.339
	0.472	5.1E-04	3.010	0.566	-2.6E-03	1.7E-05	2.705
	0.605	-1.8E-03	0.955	0.630	-3.3E-03	1.5E-05	0.944
1c	0.436	9.4E-05	1.530	0.391	2.0E-03	-1.4E-05	1.477
	0.541	-5.1E-03	1.008	0.480	-6.7E-04	-5.5E-05	0.954
	0.336	1.1E-03	2.120	0.421	-1.7E-03	1.6E-05	1.867
	0.499	-1.4E-03	0.763	0.528	-3.2E-03	1.8E-05	0.747
1d	0.610	-2.1E-04	1.718	0.560	2.0E-03	-1.5E-05	1.650
	0.703	-5.2E-03	0.860	0.643	-7.4E-04	-5.4E-05	0.806
	0.544	3.6E-04	2.521	0.603	1.6E-03	-1.1E-05	2.403
	0.654	-1.2E-03	0.855	0.712	4.8E-03	-3.6E-05	0.792
2a	0.013	-2.1E-05	0.076	0.013	-1.4E-05	0.0E+00	0.076
	0.023	-3.0E-04	0.043	0.011	6.2E-04	1.2E-05	0.041
	-0.012	2.0E-04	0.054	-0.009	5.7E-05	1.0E-06	0.054
	-0.003	3.1E-04	0.051	-0.016	1.1E-03	-7.0E-06	0.047
2b	0.088	7.9E-04	1.748	0.046	2.9E-03	-1.8E-05	1.708
	0.246	-2.3E-03	1.178	0.081	1.0E-02	-1.6E-04	0.792
	0.009	1.2E-03	1.539	-0.053	4.1E-03	-2.3E-05	1.445
	0.093	8.0E-04	1.313	0.012	5.5E-03	-4.6E-05	1.185
2c	0.113	-1.2E-03	1.772	0.071	3.4E-03	-1.8E-05	1.733
	0.302	2.4E-03	1.223	0.128	1.1E-02	1.7E-04	0.792
	0.049	1.4E-03	1.463	-0.009	4.1E-03	-2.1E-05	1.381

2d	0.147	6.6E-04	1.443	0.079	4.6E-03	-3.8E-05	1.354
2a	0.193	-9.0E-04	1.222	0.160	2.6E-03	-1.4E-05	1.198
2b	0.325	1.7E-03	0.840	0.186	8.8E-03	1.4E-04	0.568
2c	0.129	1.2E-03	1.032	0.082	3.4E-03	-1.7E-05	0.979
2d	0.201	7.5E-04	1.011	0.141	4.2E-03	-3.4E-05	0.942
3a	0.073	-2.0E-04	0.276	0.078	-4.5E-04	2.0E-06	0.275
3b	0.081	-9.7E-04	0.055	0.106	-2.9E-03	2.5E-05	0.046
3c	0.057	-1.1E-05	0.249	0.038	7.8E-04	-6.0E-06	0.240
3d	0.107	-8.7E-04	0.103	0.105	-7.6E-04	-1.0E-06	0.103
3a	0.451	2.0E-04	4.396	0.359	4.9E-03	-4.0E-05	4.207
3b	0.698	-6.8E-03	0.534	0.775	-1.3E-02	7.9E-05	0.452
3c	0.398	6.1E-04	3.976	0.118	1.3E-02	-8.6E-05	1.900
3d	0.713	-4.3E-03	1.636	0.651	-1.3E-03	-2.4E-05	1.546
3a	0.298	5.9E-04	2.657	0.231	4.0E-03	-2.9E-05	2.557
3b	0.506	-4.9E-03	0.298	0.562	-9.2E-03	5.8E-05	0.254
3c	0.241	1.0E-03	2.599	0.008	1.1E-02	-7.2E-05	1.171
3d	0.530	-3.3E-03	0.790	0.485	-1.1E-03	-1.7E-05	0.743
3a	0.495	3.6E-04	2.935	0.424	3.9E-03	-3.1E-05	2.826
3b	0.692	-4.9E-03	0.287	0.747	-9.2E-03	5.7E-05	0.244
3c	0.419	1.0E-03	2.902	0.164	1.2E-02	-7.8E-05	1.189
3d	0.695	-3.0E-03	0.747	0.633	-1.4E-05	-2.4E-05	0.655
4a	0.052	3.3E-04	0.434	0.114	-2.2E-03	1.7E-05	0.328
4b	0.072	2.3E-04	0.127	0.090	-8.7E-04	1.2E-05	0.122
4c	0.057	1.8E-04	0.343	0.028	1.2E-03	-6.0E-06	0.317
4d	0.046	1.6E-04	0.254	0.064	-7.3E-04	8.0E-06	0.247
4a	0.325	2.3E-03	3.786	0.453	-3.0E-03	3.6E-05	3.333
4b	0.469	8.1E-04	1.830	0.478	2.5E-04	6.0E-06	1.829
4c	0.511	5.8E-04	4.745	0.439	3.2E-03	-1.6E-05	4.580
4d	0.374	1.5E-04	3.927	0.245	6.6E-03	-5.5E-05	3.561
4a	0.147	1.8E-03	1.638	0.232	-1.7E-03	2.4E-05	1.437
4b	0.260	2.6E-04	0.943	0.261	2.4E-04	0.0E+00	0.943
4c	0.281	3.9E-04	2.219	0.237	2.0E-03	-1.0E-05	2.157
4d	0.140	2.7E-03	2.218	0.148	2.3E-03	3.0E-06	2.217
4a	0.420	2.0E-03	2.838	0.462	2.8E-04	1.2E-05	2.790
4b	0.580	-2.9E-04	1.455	0.591	-1.0E-03	7.0E-06	1.453
4c	0.595	1.4E-04	3.842	0.527	2.6E-03	-1.5E-05	3.697
4d	0.326	2.7E-03	2.614	0.327	2.7E-03	0.0E+00	2.614
5a	0.046	1.6E-04	0.254	0.064	-7.3E-04	8.0E-06	0.247
5b	0.091	-4.5E-04	0.202	0.082	2.0E-04	-8.0E-06	0.201
5c	0.106	-2.7E-04	0.364	0.157	-2.2E-03	1.2E-05	0.285
5d	0.094	-4.0E-05	0.441	0.077	8.1E-04	-7.0E-06	0.434
5a	0.374	1.5E-04	3.927	0.245	6.6E-03	-5.5E-05	3.561
5b	0.578	-2.4E-03	1.705	0.601	-4.0E-03	1.9E-05	1.697
5c	0.508	4.1E-04	3.162	0.596	-2.9E-03	2.1E-05	2.930
5d	0.612	-2.3E-03	2.966	0.634	-3.4E-03	1.0E-05	2.955
5a	0.140	2.7E-03	2.218	0.148	2.3E-03	3.0E-06	2.217
5b	0.427	-1.4E-03	1.215	0.440	-2.3E-03	1.1E-05	1.212
5c	0.353	9.7E-04	2.129	0.424	-1.7E-03	1.7E-05	1.977
5d	0.477	-1.9E-03	1.940	0.492	-2.7E-03	7.0E-06	1.935
5a	0.326	2.7E-03	2.614	0.327	2.7E-03	0.0E+00	2.614
5b	0.607	-1.4E-03	1.616	0.589	-7.7E-05	-1.5E-05	1.610
5c	0.542	9.4E-04	2.154	0.604	-1.4E-03	1.5E-05	2.038
5d	0.669	-1.9E-03	2.164	0.724	-4.7E-03	2.4E-05	2.096
6a	0.041	-3.6E-05	0.217	0.020	1.0E-03	-9.0E-06	0.206
6b	0.062	-2.2E-04	0.052	0.087	-2.0E-03	2.2E-05	0.043
6c	0.003	5.1E-04	0.129	0.001	5.9E-04	-1.0E-06	0.129
6d	0.045	2.8E-05	0.208	0.040	3.2E-04	-3.0E-06	0.208
6a	0.364	3.8E-04	4.056	0.268	5.1E-03	-3.9E-05	3.846
6b	0.549	-7.3E-04	1.096	0.576	-2.7E-03	2.4E-05	1.085
6c	0.216	3.2E-03	2.101	0.264	1.1E-03	1.5E-05	2.041
6d	0.552	-1.8E-03	2.657	0.652	-7.4E-03	5.4E-05	2.463
6a	0.290	5.2E-04	3.318	0.213	4.3E-03	-3.1E-05	3.184
6b	0.421	4.1E-04	0.939	0.430	-2.4E-04	8.0E-06	0.938
6c	0.157	3.2E-03	1.715	0.206	1.1E-03	1.5E-05	1.653
6d	0.467	-1.7E-03	2.301	0.549	-6.3E-03	4.5E-05	2.167
6a	0.455	3.9E-04	3.018	0.379	4.1E-03	-3.1E-05	2.886
6b	0.573	2.1E-04	1.079	0.586	-7.4E-04	1.2E-05	1.076
6c	0.339	2.8E-03	1.778	0.385	7.7E-04	1.4E-05	1.723
6d	0.605	-1.6E-03	2.159	0.666	-5.0E-03	3.3E-05	2.085

Table 3. Parameters of polynomials and the residuals of the sample crowns spectral reflectance factor of the pixels along transects.

Finally, the ANOVA was performed based on residuals of average, Linear and quadratic polynomials which parameters are shown in Table 2 and Table 3. The results of trend analysis are presented in Table 4.

transect	Linear polynomial	Fc = 3.84	Quadratic polynomial	Fc = 3.0
	Fcalculated	H0	Fcalculated	H0
1 (550nm)a	4.05	accepted	2.03	rejected
1 (550nm)b	67.03	accepted	33.09	accepted
1 (550nm)c	76.38	accepted	47.48	accepted
1 (550nm)d	2.66	rejected	1.76	rejected
1 (660nm)a	3.5	rejected	5.63	accepted
1 (660nm)b	98.72	accepted	55.53	accepted
1 (660nm)c	7.4	accepted	14.08	accepted
1 (660nm)d	23.36	accepted	12.25	accepted
1 (720nm)a	0.18	rejected	2.56	rejected
1 (720nm)b	85.81	accepted	46.97	accepted
1 (720nm)c	47.87	accepted	39.05	accepted
1 (720nm)d	17.34	accepted	9.78	accepted
1 (800nm)a	0.77	rejected	3.22	accepted
1 (800nm)b	102.54	accepted	56.58	accepted
1 (800nm)c	4.42	accepted	6.65	accepted
1 (800nm)d	12.47	accepted	10.39	accepted
2 (550nm)a	0.09	rejected	0.04	rejected
2 (550nm)b	5.94	accepted	4.97	accepted
2 (550nm)c	15.04	accepted	7.73	accepted
2 (550nm)d	16.27	accepted	12.24	accepted
2 (660nm)a	5.52	accepted	4.12	accepted
2 (660nm)b	13.11	accepted	27.71	accepted
2 (660nm)c	20.8	accepted	15.02	accepted
2 (660nm)d	4.26	accepted	7.67	accepted
2 (720nm)a	12.89	accepted	7.83	accepted
2 (720nm)b	13.05	accepted	30.06	accepted
2 (720nm)c	28.69	accepted	18.73	accepted
2 (720nm)d	2.7	rejected	4.68	accepted
2 (800nm)a	10.21	accepted	6.29	accepted
2 (800nm)b	9.65	accepted	24.81	accepted
2 (800nm)c	30.8	accepted	19.43	accepted
2 (800nm)d	4.96	accepted	6.26	accepted
3 (550nm)a	2.09	rejected	1.14	rejected
3 (550nm)b	44.12	accepted	32.31	accepted
3 (550nm)c	0.01	rejected	2.57	rejected
3 (550nm)d	137.3	accepted	68.22	accepted
3 (660nm)a	0.14	rejected	2.6	rejected
3 (660nm)b	221.21	accepted	135.31	accepted
3 (660nm)c	2.78	rejected	76.65	accepted
3 (660nm)d	206.95	accepted	112.09	accepted
3 (720nm)a	1.94	rejected	3.21	accepted
3 (720nm)b	202.58	accepted	123.34	accepted
3 (720nm)c	11.44	accepted	94.92	accepted
3 (720nm)d	258.08	accepted	139.9	accepted
3 (800nm)a	0.64	rejected	2.51	rejected
3 (800nm)b	214	accepted	129.97	accepted
3 (800nm)c	10.75	accepted	110.25	accepted
3 (800nm)d	230.16	accepted	138.69	accepted
4 (550nm)a	8.96	accepted	29.02	accepted
4 (550nm)b	2.63	rejected	3.39	accepted
4 (550nm)c	5.67	accepted	9.61	accepted
4 (550nm)d	5.25	accepted	2.72	rejected
4 (660nm)a	48.43	accepted	36.98	accepted
4 (660nm)b	2.29	rejected	1.17	rejected
4 (660nm)c	4.37	accepted	5.17	accepted
4 (660nm)d	6.28	accepted	3.85	accepted
4 (720nm)a	67.78	accepted	48.28	accepted
4 (720nm)b	0.46	rejected	0.23	rejected
4 (720nm)c	4.21	accepted	4.48	accepted
4 (720nm)d	7.52	accepted	3.98	accepted
4 (800nm)a	49.37	accepted	26.13	accepted
4 (800nm)b	0.37	rejected	0.25	rejected
4 (800nm)c	0.3	rejected	3.34	accepted
4 (800nm)d	2.44	rejected	1.42	rejected

5 (550nm)a	1.6	rejected	2.4	rejected
5 (550nm)b	3.96	accepted	2.24	rejected
5 (550nm)c	10.35	accepted	28.14	accepted
5 (550nm)d	0.06	rejected	0.85	rejected
5 (660nm)a	0.09	rejected	5.92	accepted
5 (660nm)b	13.89	accepted	7.09	accepted
5 (660nm)c	2.71	rejected	7.6	accepted
5 (660nm)d	27.68	accepted	13.98	accepted
5 (720nm)a	50.75	accepted	25.2	accepted
5 (720nm)b	6.58	accepted	3.35	accepted
5 (720nm)c	22.44	accepted	17.95	accepted
5 (720nm)d	29.12	accepted	14.64	accepted
5 (800nm)a	42.65	accepted	21.14	accepted
5 (800nm)b	4.63	accepted	2.45	rejected
5 (800nm)c	21.15	accepted	15.49	accepted
5 (800nm)d	26.08	accepted	15.19	accepted
6 (550nm)a	0.1	rejected	2.92	rejected
6 (550nm)b	3.12	rejected	10.44	accepted
6 (550nm)c	57.75	accepted	28.74	accepted
6 (550nm)d	0.04	rejected	0.15	rejected
6 (660nm)a	0.62	rejected	3.51	accepted
6 (660nm)b	1.68	rejected	1.25	rejected
6 (660nm)c	139.64	accepted	73.26	accepted
6 (660nm)d	11.21	accepted	9.97	accepted
6 (720nm)a	1.41	rejected	3.18	accepted
6 (720nm)b	0.62	rejected	0.36	rejected
6 (720nm)c	172.08	accepted	91.12	accepted
6 (720nm)d	11.29	accepted	9.06	accepted
6 (800nm)a	0.87	rejected	3.12	accepted
6 (800nm)b	0.15	rejected	0.17	rejected
6 (800nm)c	122.84	accepted	65.05	accepted
6 (800nm)d	10.75	accepted	7.3	accepted

Table 4. Trend analysis results for 550 nm, 660 nm, 720 nm and 800 nm: Fc is the critical value for the highest freedom degree in the denominator and 1 or 2 for the numerator according to the polynomial degree. Fcalculated for each hypothesis test between the average against linear and quadratic polynomials and H0 has the conclusion for each hypothesis test. Fields filled by grey are accepted in a Sequential Analysis of Variance.

The transect direction “a” was considered without linear trend by the highest number of tests. It indicates this is a direction that was better calibrated. But, the transect direction “c” presented the highest number of linear and quadratic trend. These differences can be related to the crown shape and solar illumination angle at the aerial surveying.

The 550 nm wavelength presented the lower number of accepted trend, it was 11 quadratic polynomials and 10 linear which were rejected. Then, the algorithm performed better to this wavelength than the others. The samples which represent 660 nm, 720 nm and 800 nm were accepted as presenting quadratic trend as follows: 21, 21 and 19. Quadratic trend could be a result related to the shape of crowns.

The analysis of variance accepted 65 linear polynomials as trend and 74 quadratic ones as well. But another comparison between Linear and quadratic polynomials accepted 20 linear polynomials as trend while 41 quadratic ones. These accepted polynomials as a trend were shown in the Table 3 with the cell fulfilled in gray. The number of radiometric values along transects presenting trend is higher than half of the transect samples evaluated. The total amount of transect which do not presented trend were 18. However, it is also noted the highest absolute value of the linear polynomial angular coefficient was 0.00319 with -0.00024 as average value, which is almost zero. The highest absolute value of the first order term quadratic polynomial coefficient (a1) was 0.0126 and the second order

term (a2) was 0.000169, which denote low radiometric trend on the plant crowns.

4. CONCLUSION

This study evaluated 96 transects considering 4 different directions and 4 different wavelengths. There were spectral and direction selectivity to the radiometric calibration. It was concluded that more than half of radiometric samples had trend, but the low values of coefficients showed that these trends are too smooth which could not affect spectral analysis of plants in a permanent kind of agricultural production.

Reason for these trends was that current model does not compensate for the impacts of the sky view factor and the terrain slope when the object topography is highly varying. In the future the model will be enhanced in order to obtain accurate calibration also in this type of environment.

5. ACKNOWLEDGEMENT

This research has been jointly funded by the São Paulo Research Foundation (FAPESP – grant 2013/50426-4) and Academy of Finland – decision number 273806) as well by the AGT-Bravium-Fundunesp.

REFERENCES

- Bréon, F. M., & Vermote, E., 2012. Correction of MODIS surface reflectance time series for BRDF effects. *Remote Sensing of Environment*, 125, pp. 1-9.
- Hakala, T., Honkavaara, E., Saari, H., Mäkynen, J., Kaivosoja, J., Pesonen, L., and Pölonen, I., 2013. Spectral imaging from UAVs under varying illumination conditions. *International Archives of the Photogrammetry, Remote Sensing and Spatial Information Sciences, 2013 UAV-g201*, pp. 189-194.
- Honkavaara, E., Markelin, L., Rosnell, T. and Nurminen, K., 2012. Influence of solar elevation in radiometric and geometric performance of multispectral photogrammetry. *ISPRS Journal of Photogrammetry and Remote Sensing*, 67, pp. 13-26
- Honkavaara, E., Saari, H., Kaivosoja, J., Pölonen, I., Hakala, T., Litkey, P., Mäkynen, J. and Pesonen, L., 2013. Processing and Assessment of Spectrometric. Stereoscopic Imagery Collected Using a Lightweight UAV Spectral Camera for Precision Agriculture. *Remote Sensing*, 5(10), pp. 5006-5039
- Jakob, S., Zimmermann, R. and Gloaguen, R., 2017. The Need for Accurate Geometric and Radiometric Corrections of Drone-Borne Hyperspectral Data for Mineral Exploration: MEPHySTo—A Toolbox for Pre-Processing Drone-Borne Hyperspectral Data. *Remote Sensing*, 9(1), pp. 1-17.
- Li, X. and Strahler, A. H., 1986. Geometric-optical bidirectional reflectance modeling of a conifer forest canopy. *IEEE Transactions on Geoscience and Remote Sensing*, (6), pp. 906-919.
- Markelin, L., Honkavaara, E., Peltoniemi, J., Ahokas, E., Kuitinen, R., Hyypä, J., Suomalainen, J. and Kukko, A., 2008. Radiometric calibration and characterization of large-format digital photogrammetric sensors in a test field. *Photogrammetric Engineering & Remote Sensing*, 74(12), pp. 1487-1500.

Näsi, R., Honkavaara, E., Tuominen, S., Saari, H., Pölönen, I., Hakala, T., Viljanen N., Soukkamäki, J., Näkki, I., Ojanen, H. and Reinikainen, J., 2016. UAS based tree species identification using the novel FPI based hyperspectral cameras in visible, NIR and SWIR spectral ranges. In: *International Archives of the Photogrammetry, Remote Sensing and Spatial Information Sciences, 2016 ISPRS Congress*, pp. 1143-1148.

Oliveira, R. A., Tommaselli, A. M., and Honkavaara, E., 2016. Geometric Calibration of a Hyperspectral Frame Camera. *The Photogrammetric Record*, 31 (155), pp. 325-347.

Peltoniemi, J. I., Piironen, J., Näränen, J., Suomalainen, J., Kuittinen, R., Markelin, L. and Honkavaara, E., 2007. Bidirectional reflectance spectrometry of gravel at the Sjököulla test field. *ISPRS Journal of Photogrammetry and Remote Sensing*, 62(6), pp. 434-446.

Pros. A., Colomina. I., Navarro. J.A., Antequera. R. and Andrial. P., 2013. Radiometric block adjustment and digital radiometric model generation. In: *The International Archives of the Photogrammetry. Remote Sensing and Spatial Information Sciences*. Hannover. Germany. Vol. XL-1/W1. pp. 21-24.

Smith, G. M. and Milton, E. J., 1999. The use of the empirical line method to calibrate remotely sensed data to reflectance. *International Journal of Remote Sensing*, v. 20, p. 2653-2662.

Vermote. E., Justice. C. O. and Bréon. F.-M., 2009. Towards a Generalized Approach for Correction of the BRDF Effect in MODIS Directional Reflectances. *IEEE Transactions on geoscience and remote sensing*, 47(3), pp. 898-908.

Walthall. C.L., Norman. J.M., Welles. J.M., Campbell. G. and Blad. B. L., 1985. Simple equation to approximate the bidirectional reflectance from vegetative canopies and bare soil surfaces. *Appl. Opt*, 24, pp. 383-387.